Inorganic Chemistry

Article

pubs.acs.org/IC

# Key Hydride Vibrational Modes in [NiFe] Hydrogenase Model Compounds Studied by Resonance Raman Spectroscopy and Density Functional Calculations

Hannah S. Shafaat, Katharina Weber, Taras Petrenko, Frank Neese, and Wolfgang Lubitz*

Max Planck Institute for Chemical Energy Conversion, Stiftstrasse 34-36, D-45470 Mülheim an der Ruhr, Germany

Supporting Information

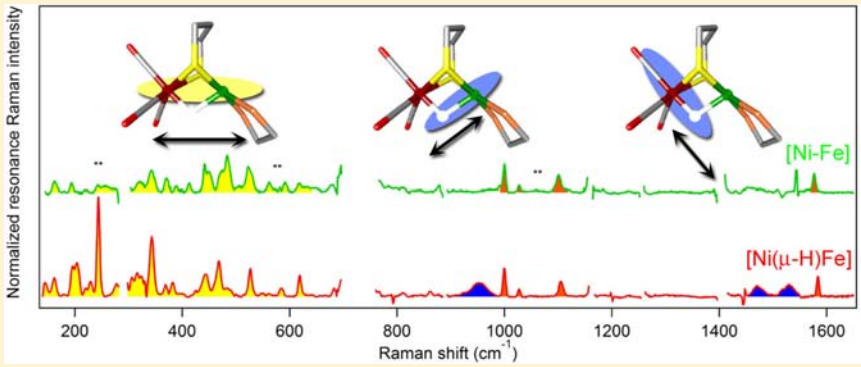


**ABSTRACT:** Hydrogenase proteins catalyze the reversible conversion of molecular hydrogen to protons and electrons. While many enzymatic states of the [NiFe] hydrogenase have been studied extensively, there are multiple catalytically relevant EPR-silent states that remain poorly characterized. Analysis of model compounds using new spectroscopic techniques can provide a framework for the study of these elusive states within the protein. We obtained optical absorption and resonance Raman (RR) spectra of (dppe)Ni($\mu$-pdt)Fe(CO)$_3$ and [(dppe)Ni($\mu$-pdt)($\mu$-H)Fe(CO)$_3$][BF$_4$], which are structural and functional model compounds for the EPR-silent Ni−SI and Ni−R states of the [NiFe] hydrogenase active site. The studies presented here use RR spectroscopy to probe vibrational modes of the active site, including metal−hydride stretching vibrations along with bridging ligand−metal and Fe−CO bending vibrations, with isotopic substitution used to identify key metal−hydride modes. The metal−hydride vibrations are essentially uncoupled and represent isolated, localized stretching modes; the iron−hydride vibration occurs at 1530 cm$^{-1}$, while the nickel−hydride vibration is observed at 945 cm$^{-1}$. The significant discrepancy between the metal−hydride vibrational frequencies reflects the slight asymmetry in the metal−hydride bond lengths. Additionally, time-dependent density functional theory (TD-DFT) calculations were carried out to obtain theoretical RR spectra of these compounds. On the basis of the detailed comparison of theory and experiment, the dominant electronic transitions and significant normal modes probed in the RR experiments were assigned; the primary transitions in the visible wavelengths represent metal-to-metal and metal-to-ligand charge transfer bands. Inherent properties of metal−hydride vibrational modes in resonance Raman spectra and DFT calculations are discussed together with the prospects of observing such vibrational modes in metal−hydride-containing proteins. Such a combined theoretical and experimental approach may be valuable for characterization of analogous redox states in the [NiFe] hydrogenases.

## INTRODUCTION

Hydrogen has been proposed as one of the leading candidates for carbon-free energy storage; as a clean-burning fuel, it possesses high energy density and can be used as a feedstock to produce other fuels.[1] Therefore, hydrogen production has been the focus of extensive research over the last few decades. In nature, hydrogen is a key metabolite for many types of microbes, including soil bacteria and extremophiles, through application of specialized proteins called hydrogenases.[2] There are three types of hydrogenases—[FeFe], [NiFe], and [Fe]—each with a metal-based active site and unique organometallic ligands.[3] The more prevalent [NiFe] hydrogenases contain a redox-active nickel center that plays a critical role in hydrogen binding,[4] and considerable progress has been made toward understanding the enzymatic mechanism, particularly for the EPR-active redox states.[3,5−8] However, of the three proposed catalytically relevant states (shown in Figure 1), only one is paramagnetic—the Ni−C state with the oxidation states of Ni(III)Fe(II) in the active site. This state has been found to contain a nearly symmetric bridging hydride between the two metals in what was previously known as the "open" coordination site from crystallography studies.[5,7−9] The electronic and geometric structure of the other two states,

Received: August 6, 2012
Published: October 5, 2012

   dx.doi.org/10.1021/ic3017276 | Inorg. Chem. 2012, 51, 11787−11797

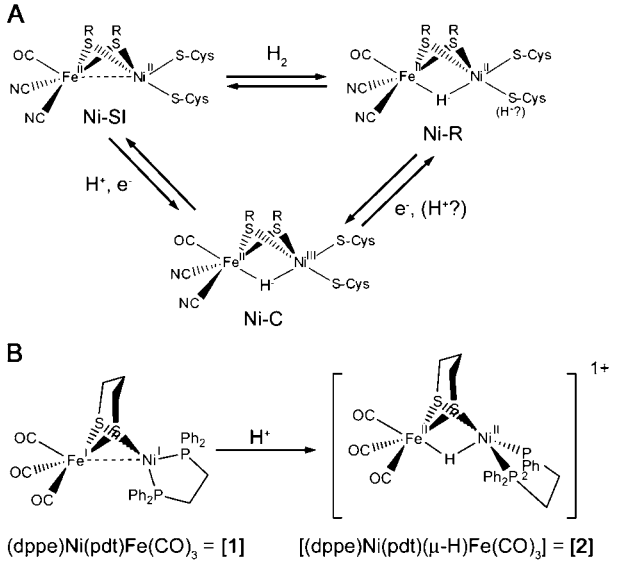


**Figure 1.** (A) Proposed catalytic cycle and structures of intermediates of the [NiFe] hydrogenase active site in the EPR-silent, active (Ni–SI), reduced EPR-active (Ni–C), and EPR-silent, reduced (Ni-R) states.[10] (B) Structural models **1** and **2** for the [NiFe] hydrogenase active site in the corresponding EPR-silent states.

the Ni–SI and Ni–R states, are thought to contain Fe(II)Ni(II) and are largely uncharacterized due to the lack of structural data or appropriate spectroscopic techniques to yield electronic information.[3,4,10]

Along with detailed studies to understand the mechanism at play in the protein systems, significant progress has been made synthesizing and characterizing small-molecule models of the active sites of hydrogenases.[11−15] These models are of general interest for two primary reasons: (1) they can provide insight into the structure and therefore mechanism of action of the proteins, and (2) they may be used in technological applications for hydrogen fuel generation. Structural models with bridging thiolate ligands, carbonyl and/or cyanide terminal ligands on iron, and amine, phosphine, or biologically relevant thiolate terminal ligands on the nickel center reproduce the Ni–Fe and M–$S_{bridge}$ distances observed in the protein crystal structures;[11,12] one molecule even accurately reproduces the FTIR frequencies of the *A. vinosum* [NiFe] hydrogenase protein.[16] However, most of the molecules which reproduce the structure of the protein are catalytically inactive, due to the lack of accessible coordination sites around iron. By contrast, electrocatalytically active models of hydrogenase historically have included either mononuclear nickel–phosphine compounds or trinuclear nickel–iron clusters.[11,12,17−19] Recently, however, a hydride-bridged heterobimetallic model has been developed that is both a structural and a functional mimic of the hydrogenase active site.[20] The thiolate-bridged (dppe)Ni($\mu$-pdt)Fe(CO)$_3$, **1**, demonstrates Ni–Fe distances similar to those observed in the protein (2.59 Å in the reduced protein vs 2.61 Å in **1**)[20,21] and possesses a metal–metal bond that may be relevant in the protein system as well.[22,23] This EPR-silent compound serves as a model for the catalytically relevant Ni–SI state in the protein, which is thought to lack one ligand between the two metal centers. The metal–metal bond in **1** can be protonated to form a stable, hydride-bridged molecule, [(dppe)Ni($\mu$-pdt)($\mu$-H)Fe(CO)$_3$][BF$_4$], **2**.[13,20] Under acidic conditions, **2** electrocatalytically produces hydrogen with an overpotential of ∼310 mV.[13,20] This molecule is also EPR silent, with oxidation states of +2 on both metal sites, and therefore can be considered a structural and an electronic mimic of the most reduced state of the protein, Ni–R. The structures of these molecules are shown in Figure 1 and compared to the protein active site catalytic intermediates.

While the [NiFe] hydrogenase absorption spectrum is dominated by the three iron–sulfur clusters in the protein, these model compounds exhibit strong near-UV absorption bands as well as moderate absorption bands in the visible region of the spectrum, rendering them prime candidates for characterization by resonance Raman (RR) spectroscopy. Because of the sensitive and selective nature of this method, RR has been extensively applied to the study of many different types of active sites within large proteins, since interference from the protein backbone, solvent, and even other chromophores such as iron–sulfur clusters can be largely avoided by tuning the excitation wavelength.[24] Raman spectroscopy has also been used to characterize the iron–carbonyl modes and iron–hydride stretch in [FeFe] hydrogenase model compounds.[25−27] It is important to note that vibrational spectroscopy allows observation of bound protons and hydrides, often under physiologically relevant conditions, which is generally beyond the capabilities of many spectroscopic and structural techniques. Therefore, this technique holds promise for characterization of metal–hydride species within proteins, provided appropriate electronic transitions can be identified and probed.

In this work, we present the resonance Raman spectra of (dppe)Ni($\mu$-pdt)Fe(CO)$_3$, **1**, [(dppe)Ni($\mu$-pdt)($\mu$-H)Fe(CO)$_3$][BF$_4$], **2**, and the isotopically substituted derivative [(dppe)Ni($\mu$-pdt)($\mu$-D)Fe(CO)$_3$][BF$_4$], **3**, and identify distinct bands that correspond to metal–hydride vibrational modes. Analysis of the vibrational frequencies and line shapes reveals characteristics of metal–hydride vibrations that are directly correlated to molecular structure. Additionally, a detailed density functional theory (DFT) based study was carried out to determine the relevant electronic transitions and predict the resonance Raman intensities of these compounds, which greatly facilitates interpretation of the vibrational spectra. Characterization of these hydrogenase model compounds using resonance Raman spectroscopy and advanced spectroscopic calculations provides a foundation upon which to study the [NiFe] protein active site and gain structural information about the critical EPR-silent redox states.

## MATERIALS AND METHODS

**Synthesis.** Compounds **1** and **2** were synthesized as reported in the literature.[20,22] Synthesis of **3** was carried out in a J. Young NMR tube under an inert atmosphere. a 9.7 mg (0.012 mmol) amount of **2** was dissolved in 0.5 mL of $CD_2Cl_2$, and a $^1$H NMR spectrum was recorded. Then 10 $\mu$L of $D_2O$ (0.55 mmol) was added at room temperature as well as 0.1 mL of acetone-$d_6$ for better solubility. After 16 h, a $^1$H NMR spectrum was recorded and the disappearance of the hydride signal at −3.48 ppm was observed; the $^{31}$P NMR spectrum showed one signal at 70 ppm, which verified that no decomposition took place. Solvent was removed in vacuo, and **3** was isolated as an orange-red solid.

**Sample Preparation.** Samples were prepared in an anaerobic chamber (MBraun LabMaster130). Solid samples were weighed and dissolved in dichloromethane that had been dried over $CaH_2$; a series of dilutions was prepared to identify optimal sample concentrations for high signal intensity and minimal interference from self-absorption effects. A 100 $\mu$L amount of sample was transferred to EPR tubes,


dx.doi.org/10.1021/ic3017276 | *Inorg. Chem.* 2012, 51, 11787−11797

sealed with silicon stoppers, and frozen in liquid nitrogen immediately upon removal from the anaerobic chamber. No sample decomposition was observed over this time scale prior to freezing.

**Spectroscopy.** Absorption spectra of **1** and **2** were obtained using a diode-array UV−vis spectrometer (HP 8453). Serial dilutions of samples were prepared in an anaerobic chamber. Absorption spectra were measured in 2 mm path length cuvettes sealed with a silicon stopper to retain anaerobic conditions, and spectra were measured quickly (<2 min) after removing from the anaerobic chamber to avoid decomposition; no changes in the absorption spectra were observed over the time scale of these measurements. Averages of 3 dilutions were considered to obtain accurate extinction coefficients considering only points within the linear range of the instrument (0.005−1 au). Absorption spectra were decomposed into Gaussian bands using the orca_asa program[28] in order to obtain the transition energies, oscillator strengths, and broadening parameters presented in the table in the Supporting Information. Spectra were fit to the fewest number of bands necessary to reproduce all features in the absorption spectrum.

Resonance Raman spectra of samples containing 1.4 mM **1**, 5 mM **2**, and 5 mM **3** in dichloromethane were obtained using the 488 and 514.5 nm excitation lines from a $Kr^+/Ar^+$ ion laser (Spectra Physics BeamLok 2060 6S); a diffraction grating was used to remove laser side bands. Power at the sample was ∼50 mW. Sample was contained in a quartz EPR tube within an EPR quartz finger dewar and cooled using liquid nitrogen. Raman-scattered light was collected in a 180° backscattering geometry using a 100 mm diameter *f*/1.5 lens and focused onto the entrance slit of a spectrograph with a 100 mm diameter *f*/4 lens; a polarization scrambler was used in front of the spectrograph to account for the polarization dependence of the collection and detection optics. The scattered light was dispersed with a triple monochromator (Acton Research TriplePro) equipped with 600, 1200, and 2400 gr/mm holographic gratings and imaged onto a liquid-nitrogen-cooled CCD detector (Roper Scientific SPEC10-LN). Entrance and exit slits were 50 $\mu$m, giving a bandwidth of ∼3 $cm^{-1}$. Spectra were collected for ∼4−5 cycles of 30 min each for a given wavelength and spectral window; corresponding spectral windows were stitched together ensuring overlap that included at least one peak for normalization. Raman shifts were calibrated to an accuracy of 1 $cm^{-1}$ using $Na_2SO_4$ and $CCl_4$ for the low-frequency spectral region and acetone and acetonitrile for the high-frequency spectral region.[29,30] Samples were translated to avoid photoinduced artifacts every few minutes during collection, and no evidence of sample degradation, as indicated by decreased intensities of peaks, was detected. Spectra measured at 18 mW showed identical peaks but with lower signal-to-noise ratios.

**Calculations.** All calculations were carried out using the ORCA computational chemistry program.[31−33] Geometry optimizations and spectroscopic analysis were performed with the BP86[34,35] and B3LYP[36,37] functionals for density functional theory. The def2-TZVP basis set was used for all atoms except ligand hydrogens, for which the def2-SV(P) basis set was used.[38] For the bridging hydrogen, the def2-TZVP basis set was employed. A larger basis set on the bridging hydrogen, aug-def2-TZVPP, which was derived from def2-TZVPP by augmentation with diffuse basis functions proposed by Dunning,[39] had a minor influence on the calculated geometric and spectroscopic parameters. The zero-order-relativistic-approximation was applied to all atoms;[40−42] application of the def2-TZVPP basis set to all atoms, the van der Waals correction,[43,44] and/or invoking the conductor-like screening (COSMO) model[45] did not affect either the calculated geometry or the predicted spectroscopic parameters within the error limits of the methodology. Vibrational frequencies were calculated using two-sided numerical differentiation to give the predicted off-resonance Raman and IR spectra. Time-dependent density functional (TD-DFT) calculations within the Tamm−Dancoff approximation were performed for the first 40 roots using the B3LYP functional.[46−48] Resonance Raman intensities for the relevant electronic transitions were predicted within the independent mode displaced harmonic oscillator (IMDHO) model using the normal mode gradient technique for calculating the dimensionless displacements (Δ) for each of the normal modes.[28] The orca_asa program was then used to simulate the absorption and RR spectra for first-order vibrational transitions.[28,49,50] As described in the text, normal modes could be assigned on the basis of similar frequencies and predicted vibrational intensities. The final simulated RR spectra presented in Figures 5 and 6 as well as in the Supporting Information were generated following assignment of the vibrational modes by adjusting the theoretical band frequency in the calculation input file to match the experimental frequency. Required adjustments for modes with frequencies <1500 $cm^{-1}$ were in the range from −30 to +25 $cm^{-1}$ with most adjustments within ∼10 $cm^{-1}$; adjustments for high-frequency modes scaled appropriately with the anticipated B3LYP scaling factor of ∼96−97%.[51,52] The one exception to this is the Fe−H stretching mode, $\nu_{182}$; this discrepancy is discussed further below. Scans of the potential energy surfaces along individual normal modes for predicting anharmonic parameters were implemented using the NMScan module within ORCA.

## RESULTS

**Spectroscopic Characterization.** *Electronic Absorption Spectroscopy.* These hydrogenase model compounds exhibit strong near-ultraviolet and visible absorption bands as evidenced by their visual appearance; **1** is a dark green color, while **2** appears red. Electronic absorption spectra of **1** and **2** are shown in Figure 2. The spectrum of **1** contains two lower

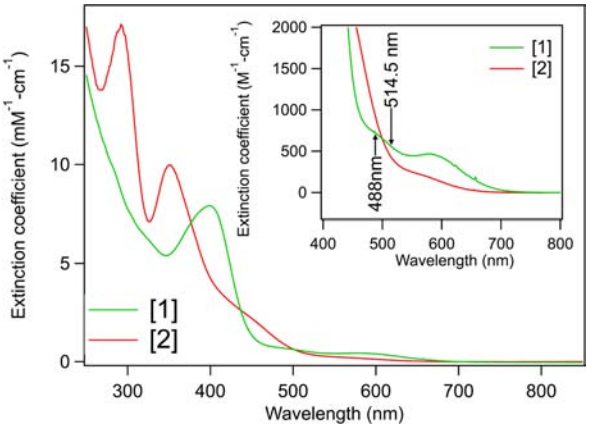


**Figure 2.** Absorption spectra of **1** and **2** in dichloromethane. (Inset) Zoomed-in region of absorption spectra to indicate extinction coefficients in preresonant region used in resonance Raman experiments. Resonance Raman excitation wavelengths used in this study are indicated.

intensity bands at 590 ($\varepsilon \approx 650$ $M^{-1}$ $cm^{-1}$) and 500 nm ($\varepsilon \approx 800$ $M^{-1}$ $cm^{-1}$) as well as a strong absorption band at 400 nm ($\varepsilon \approx 8100$ $M^{-1}$ $cm^{-1}$). The absorption spectrum of **2** exhibits blue-shifted electronic transitions, with three primary bands: a strong transition at 350 nm ($\varepsilon \approx 10\,000$ $M^{-1}$ $cm^{-1}$), a shoulder at 450 nm ($\varepsilon \approx 2200$ $M^{-1}$ $cm^{-1}$), and a broad, weak feature around 575 nm ($\varepsilon \approx 200$ $M^{-1}$ $cm^{-1}$). An additional, intense band at 290 nm is also observed.

*Resonance Raman spectroscopy.* RR spectra of **1** and **2** measured using 488 nm excitation are compared to the FTIR spectra in Figure 3. RR spectra of both species are dominated by high-intensity, low-frequency bands (<600 $cm^{-1}$), shaded in yellow. Most notably, the RR spectrum of the hydride-bridged compound **2** exhibits broad bands at 950, 1470, and 1530 $cm^{-1}$, indicated on the graph with blue shading, which are absent in the spectrum of **1**. There are three bands at 1000, 1026, and 1104 $cm^{-1}$ (shaded in orange) that remain essentially unchanged in frequency, line width, and relative intensity


dx.doi.org/10.1021/ic3017276 | Inorg. Chem. 2012, 51, 11787−11797

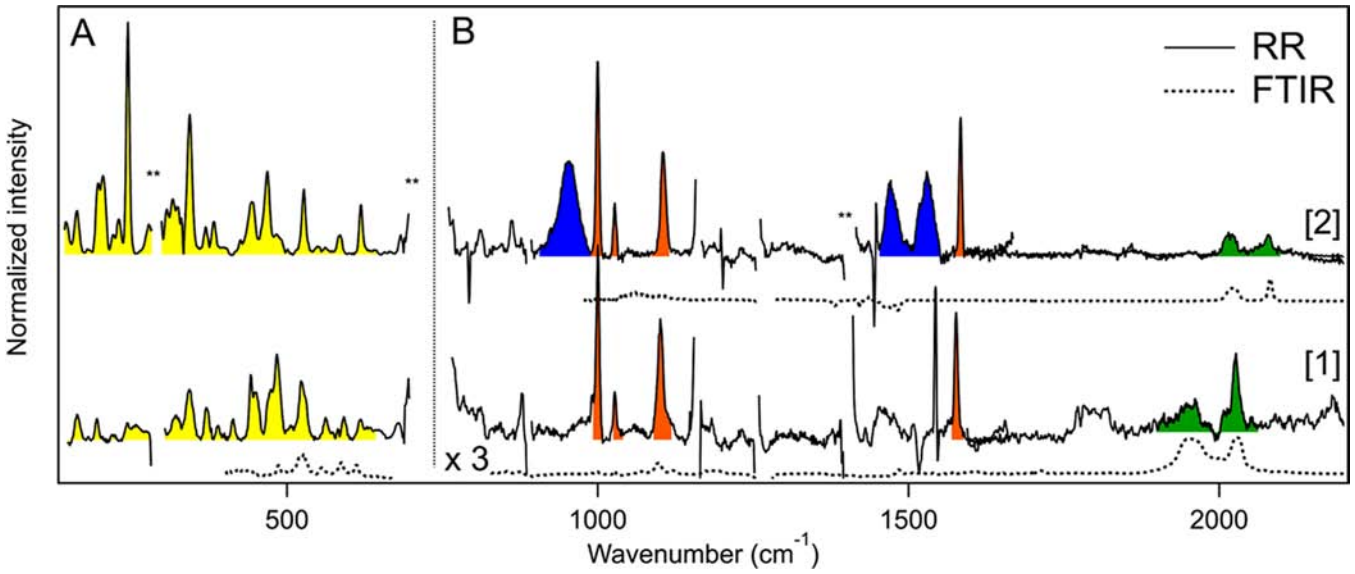


**Figure 3.** Resonance Raman (488 nm excitation, 77 K, solid lines) and FTIR spectra (295 K, dotted lines) of **1** and **2** in dichloromethane. Shading of vibrational bands discussed in text. Regions obscured by large solvent peaks have been removed for clarity and indicated with **. RR spectra are normalized to the peak intensity at 1000 $cm^{-1}$. FTIR spectra are normalized to maximum intensity ≈ 2000 $cm^{-1}$. All traces in B have intensities multiplied by 3 for clarity. Savitsky–Golay smoothing algorithm has been applied to the high-frequency region (1700–2200 $cm^{-1}$) of the RR spectra.

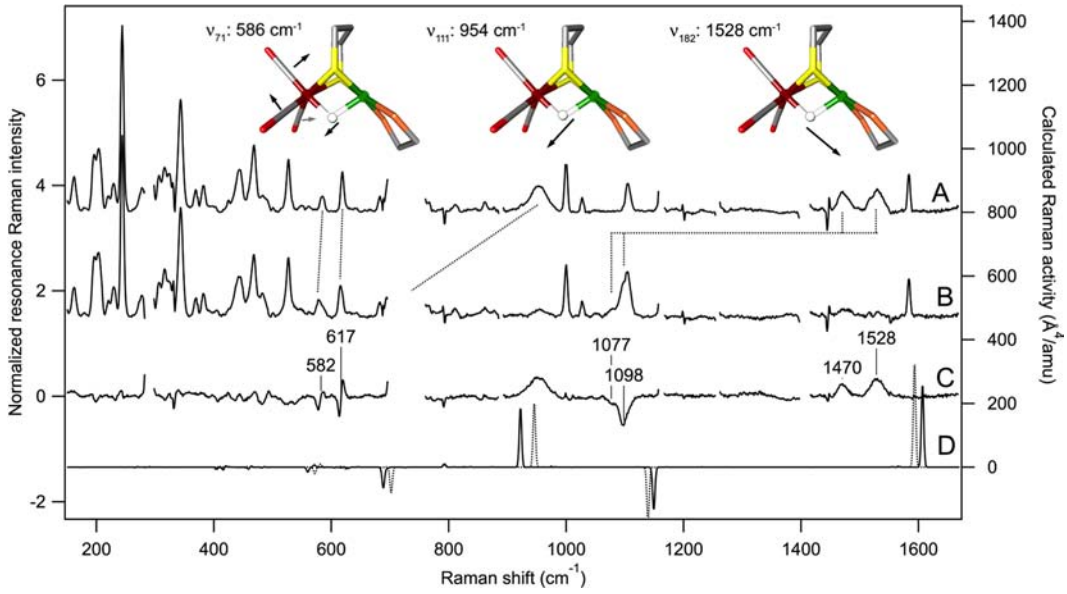


**Figure 4.** Resonance Raman spectra (488 nm excitation, 77 K) of (A) 5 mM **2**, (B) 5 mM **3**, (C) difference spectrum of **2** − **3**, and (D) calculated (B3LYP/def2-TZVP) Raman difference spectrum of **2** − **3** (solid line) and **2′** − **3′** (dotted line). Frequencies for D are scaled by 0.96 to account for systematic errors in B3LYP-calculated frequencies. Regions obscured by strong solvent peaks are removed for clarity. Dominant difference peaks in C are labeled for each isomer. (Inset) Schematic depictions of vibrational modes with significant hydride displacements. Structure shown represents optimized geometry of **2** from DFT calculations (B3LYP/def2-TZVP). Hydrogen atoms on ligands are omitted for clarity. Experimental frequencies for **2** are given for each mode.

between the spectra of **1** and **2**. In addition, sharp peaks at 1575 and 1583 $cm^{-1}$ are found in **1** and **2**, respectively. The high-frequency regions of the RR spectra show weak, broad bands around metal–carbonyl stretching frequencies, shaded in green. Frequencies and bandwidths of the carbonyl stretching modes observed in the RR spectra show good agreement with the frequencies and bandwidths observed in the FTIR experiment (shown as dotted lines) and the literature values.[20,22] Resonance Raman spectra obtained using multiple excitation wavelengths (488 and 514.5 nm) exhibit slight changes in relative band intensities (Figure S1, Supporting Information).

RR spectra of **1** and **2** reveal frequencies and intensities that are consistent with predicted expectations for inorganic small molecule complexes; therefore, preliminary analyses of these spectra allow for general interpretation of the bands. Low-frequency, high-intensity bands are typical for metal–metal- and metal–ligand-derived normal modes. Due to the lack of symmetry in the investigated molecules, there are ∼50 predicted modes and ∼20 bands observed in this spectral region for both compounds. Thus, it is difficult, if not impossible, to assign the observed spectral features on the basis of DFT-calculated frequencies alone; use of calculations to


dx.doi.org/10.1021/ic3017276 | *Inorg. Chem.* 2012, 51, 11787–11797

**Table 1. Calculated and Experimental Vibrational Frequencies ($cm^{-1}$) for Predicted Normal Modes of 2 and 2′ with Significant Hydride Displacements**

| | calcd frequency | | | exptl frequency | | | |
|---|---|---|---|---|---|---|---|
| calcd mode no.[a] | 2 | 3 | calcd $\nu[3]-\nu[2]$ | 2 | 3 | exptl $\nu[3]-\nu[2]$ | mode description[b] |
| 71 | 594.1 | 582.4 | −11.7 | 585.8 | 579.4 | −6.4 | $\delta$(Fe−C−O) + $\nu$(Ni−H) + $\delta$(H−Fe−C) |
| 71′[c] | 604.7 | 594.7 | −10 | 619 | 615.4 | −3.6 | |
| 111 | 959.2 | 716.4 | −242.8 | 945.1 | ND[d] | ND | $\nu$(Ni−H) + $\delta$(H−Fe−Ni) |
| 111′ | 984.3 | 730.0 | −254.3 | 960.6 | ND | ND | |
| 182′ | 1657.3 | 1185.2 | −472.1 | 1470.1 | 1076.7 | −393.4 | $\nu$(Fe−H) + $\delta$(H−Ni−Fe) |
| 182 | 1671.5 | 1195.2 | −476.3 | 1528.4 | 1095.8 | −432.6 | |

[a]Mode numbering from calculated vibrational modes in ascending frequency order. [b]Mode descriptions are obtained from visualizing calculated vibrational trajectories and comparison to calculated bond stretching vibrations partitioned among normal modes. Bending displacements are represented with $\delta$; stretching displacements are represented with $\nu$. [c]Modes with prime (′) refer to calculations on different isomers; see text for discussion. [d]Modes $\nu_{111}$ and $\nu_{111'}$ are not determined (ND) in complex 3 because of interference from strong solvent peaks.

aid in mode assignment is discussed further below. Bands shaded in orange, which occur in a frequency range higher than expected for metal−ligand vibrations and are narrow and of higher intensity than expected for overtone or combination bands, can likely be ascribed to ligand-centered normal modes. Frequencies of the carbonyl stretching bands in the resonance Raman spectra are consistent with those observed in the FTIR experiments.[20] Intensities of these bands are greatly diminished in the RR spectra compared to the FTIR spectra due to differences in the selection rules between the two types of spectroscopy.

To identify normal modes of **2** that involve displacement of the hydride bridge, RR spectra of the H/D-exchanged compound **3** were measured. RR spectra of **2** and **3** as well as the difference spectrum are shown in Figure 4. This difference spectrum is compared to the off-resonance Raman frequency shifts calculated to occur upon isotopic substitution. Spectra of **2** and **3** are very similar, and most of the bands in the low-frequency region of the spectrum remain unchanged. However, the difference spectrum reveals small shifts in bands at 486 (−2 $cm^{-1}$ in **3**), 586 (−6 $cm^{-1}$ in **3**), and 619 $cm^{-1}$ (−4 $cm^{-1}$ in **3**). More striking are the differences observed in the midfrequency regions of the spectra. There is a strong, broad band centered around 950 $cm^{-1}$ for **2** that does not appear in the RR spectrum of **3**; a corresponding band at lower frequencies is not observed. Additionally, broad bands at 1470 and 1528 $cm^{-1}$ are observed only in the RR spectrum of **2**; new bands in the spectrum of **3** appear at 1077 and 1096 $cm^{-1}$. On the basis of these significant shifts, we can definitively state that these modes contain considerable hydride displacements; band assignments to specific normal modes were made with the help of calculations and are discussed below. To quantify the breadth of these bands, spectra were decomposed into Gaussian peaks (Figure S2 and Table S2, Supporting Information), and it was found that the average line width of the isotope-dependent peaks of **2** was more than two times greater than the line width of a representative, isotope-independent peak in the same spectral region (the band at 1105 $cm^{-1}$ was used for this comparison). Vibrational linewidths of the isotope-dependent bands are discussed further below.

Observation of two distinct, broad peaks with an approximately equal intensity ratio in the RR spectrum of **2** around 1500 $cm^{-1}$ prompted further investigation, for two peaks are also observed in the spectrum of **3** at 1077 and 1096 $cm^{-1}$. Additionally, the broad band of **2** at ∼950 $cm^{-1}$ may actually represent two overlapping bands with equal intensities and peak positions of 945 and 960 $cm^{-1}$ (Figure S2, Supporting Information). These results suggest that there may be different conformations or isomers of **2** and **3**, referred to as **2′** and **3′**, that are probed in the RR experiments. This suggestion has literature precedence, for it has previously been observed that the bridging $pdt^{2-}$ ligand can undergo ring inversion with low energetic barriers[53,54] and exist in two conformations on either side of the molecule.[54−56] This possibility is further explored with DFT calculations on each isomer, described below.

**DFT Calculations.** *Calculation of Geometric Parameters.* The geometry-optimized structures of **1** and **2** obtained using density functional theory with the B3LYP functional are generally consistent with values obtained from the X-ray crystal structures (Supporting Information, Table S1). The calculated metal−ligand and intraligand distances of **1** were mostly observed to be within ∼0.03 Å of the experimental distances;[22] the largest deviations were found for one of the metal−sulfur bond lengths on each metal, which were overestimated by ∼0.1 Å for nickel and ∼0.04 Å for iron. Notably, the metal−metal bond distance, which can be experimentally determined to high accuracy, was calculated in fortuitously exact agreement with the crystal structure. There was somewhat larger discrepancy in the calculated geometry of **2**. While intraligand distances remained consistent between the crystal structure and the calculated geometry, metal−sulfur distances were overestimated by ∼0.05 Å for both metals, the nickel−phosphine distances were overestimated by ∼0.07 A, and the nickel−iron distance was overestimated by ∼0.09 Å.[20] These are reasonable discrepancies given the weak metal−ligand bond character.[57] The most significant deviations between experiment and theory occur for the metal−hydride bond lengths, which are much longer in the calculations than observed in the crystal structure; however, it is known that X-ray diffraction structures systematically underestimate bond lengths to hydrogen atoms by ∼0.1−0.2 Å due to the electron density residing in the bond rather than around the nucleus. Accounting for this difference, there is good agreement between the calculated and experimental iron−hydride bond length but the overestimation of the nickel−hydride bond length (∼0.15 Å) remains. This difference is larger than what is expected for this type of calculation.[58] The differences between the calculated and the experimental geometries of **2** as well as the asymmetry of the hydride bridge are discussed further below.

Use of the BP86 functional for geometry optimization provides better agreement with the crystal structure, particularly for the metal−hydride distances. This is often observed in DFT calculations.[57,59] In fact, GGA functionals such as BP86 are


dx.doi.org/10.1021/ic3017276 | Inorg. Chem. 2012, 51, 11787−11797

commonly used to obtain theoretical vibrational frequencies and normal mode compositions (see Supporting Information for additional discussion).[60] However, most other spectroscopic properties as well as total energies are more accurately predicted with hybrid functionals;[60] therefore, the B3LYP results were used for analysis of the absorption and RR spectra.

*Possibility of Multiple Conformations in Solution.* To probe whether the multiple, broad bands observed in the high-frequency region of the RR spectra of **2** are due to different conformational isomers, DFT calculations were performed on **2** with an initial geometry that reflects a conformation with an inverted $pdt^{2-}$ ring. Geometry optimizations performed on this isomer of **2**, denoted **2′**, resulted in very similar structures (Figure S3, inset, Supporting Information) which are isoenergetic within the accuracy limits of the method. Frequency calculations on **2′** predict nearly identical frequencies for almost all vibrational modes, including the carbonyl stretching vibrations, with the primary differences occurring in the calculated nickel– and iron–hydride stretching vibrations, $\nu_{111}$ and $\nu_{182}$, respectively (Table 1 and Figure S3, Supporting Information, additional discussion in the Supporting Information). These results suggest that both conformations of **2** exist in frozen solution. The spectroscopic analysis below was therefore performed assuming equal contributions from **2** and **2′** to the spectra, and the band assignments to each isomer are indicated in Table 1. Throughout the text, parameters specific to the ring-inverted isomer are denoted with a prime (′).

Analogous calculations on **1** were performed with an inverted $pdt^{2-}$ ligand. The geometry-optimized structure of **1′** was very similar to **1** (Figure S4, inset, Supporting Information), and **1′** is also calculated to be essentially isoenergetic to that of **1**. In addition, the vibrational spectra are predicted to exhibit nearly identical stretching frequencies for both isomers, which indicate that for a mixture of **1** and **1′** in equilibrium in solution the RR spectra of the isomers would be indistinguishable (Figure S4, Supporting Information).

*Calculation of Vibrational Frequencies and Isotopic Shifts.* On the basis of the agreement between the calculated and the experimental frequency shifts between **2** and **3**, as shown in Figure 4, it is possible to assign these bands to normal modes of both isomers of the molecule (Table 1). A pictorial representation of the atomic displacements involved in the assigned normal modes is shown in Figure 4, inset. As expected, these modes show significant hydride displacement. The band at 586 $cm^{-1}$ can be assigned to $\nu_{71}$, which consists of a nickel–hydride stretch with an orthogonal iron–hydride bend that couples to iron carbonyl bending modes. This mode is predicted to occur at 594 $cm^{-1}$ in **2** and shift −12 $cm^{-1}$ upon H/D exchange; a −6 $cm^{-1}$ shift is observed experimentally. The band with a maximum at 953 $cm^{-1}$ can be decomposed into two, equally intense bands at 945 and 961 $cm^{-1}$ that consist primarily of nickel–hydride stretch, which is denoted $\nu_{111}$ due to the mode ordering in the calculations, while the high-frequency, broad bands at 1470 and 1528 $cm^{-1}$, denoted $\nu_{182}$ from the calculated mode ordering, reflect nearly isolated iron–hydride stretching vibrations. The iron–deuterium stretch of **2** shifts by −433 $cm^{-1}$ upon isotopic substitution, which compares well to the DFT-calculated shift of −476 $cm^{-1}$. The corresponding nickel–deuterium stretch, which is predicted to fall at 716 $cm^{-1}$, is not observed in the experimental spectrum, likely due to interference from strong solvent peaks between 680 and 760 $cm^{-1}$.

*Theoretical Prediction of Absorption and Resonance Raman Spectra of 1.* In order to better understand the nature of the electronic transitions probed in the resonance Raman experiments as well as facilitate normal mode assignments, calculations on the excited-state transitions, energies, and normal mode gradients were carried out. This procedure enables the theoretical prediction of absorption and RR spectra of **1** and **2**. Time-dependent DFT (TD-DFT) calculations on **1** give reasonable agreement between the predicted and the experimental absorption spectra; applying an energy shift of −2700 $cm^{-1}$ to the calculated transitions provides a better match (Figure 5, top).[28] A systematic error of this magnitude is

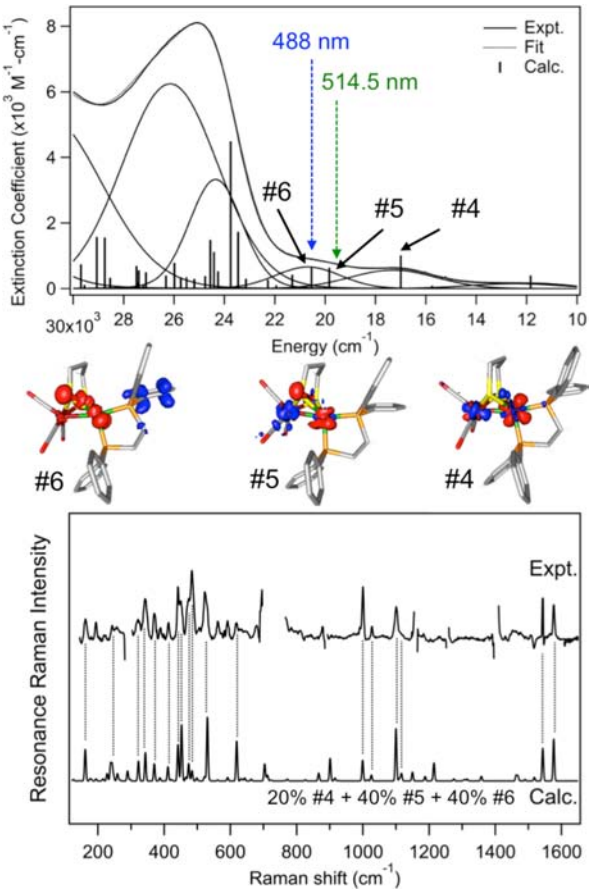


**Figure 5.** (Top) Experimental (solid line) and decomposed (dotted line) absorption spectrum of **1** and calculated TD-DFT transition energies (offset by −2700 $cm^{-1}$). Dominant electronic states probed in RR experiments as well as RR excitation wavelengths indicated on graph. (Middle) Difference density contour plots for relevant electronic transitions shown. Negative electron density in electronic transition is represented by red lobes; positive electron density is represented by blue lobes. (Bottom) Experimental (488 nm ex.) and calculated RR spectrum of **1**. Calculated spectrum represents a superposition of calculated spectra for individual excited states in the ratios indicated on the graph. Calculated line shapes are generated using a Gaussian function with a 5 $cm^{-1}$ line width.

certainly common for TD-DFT calculations. The absorption features can therefore be assigned to different electronic transitions (Figure 5, Table S3, Supporting Information). These results reveal that there are three dominant electronic transitions probed with RR excitation at 488 nm (20 500 $cm^{-1}$). Difference density plots (Figure 5, top, inset) of these transitions indicate that the lowest energy contributor, State 4,


dx.doi.org/10.1021/ic3017276 | *Inorg. Chem.* 2012, 51, 11787–11797

has significant charge transfer contributions from nickel to both phosphine and thiolate ligands, with additional electron density gained on the iron site and delocalized onto the carbonyl ligands. The second transition, State 5, has nickel to iron metal−metal charge transfer character, with contributions from thiolate-to-iron (ligand-to-metal) charge transfer (LMCT) as well. The higher energy State 6 almost exclusively represents charge transfer from the nickel−thiolate core to the phosphine phenyl ligands.

For dipole-allowed transitions, resonance Raman intensities are largely determined by the corresponding excited state normal mode displacements, which necessarily correlate with changes in the bonding pattern of the excited electronic state relative to the ground state. Thus, identifying the nature of the electronic transitions probed with RR spectroscopy can aid in vibrational mode identification. A qualitative assessment of these transitions in the absorption spectrum of **1** therefore enables one to predict that nickel−pdt and nickel−dppe modes will be observed as well as modes involving iron−carbonyl and nickel−iron displacements. Additionally, the character of State 6 indicates that vibrations due to the phenyl substituents on the phosphine ligand will be observed. These bands should exhibit narrow line shapes and are likely to resemble the Wilson-type benzene modes, which correspond to the high-intensity, high-frequency bands between 1000 and 1600 $cm^{-1}$ (shaded in orange, Figure 2). These experimental peaks can be assigned to the three calculated sets of bands ($\nu_{116}$, $\nu_{120}$, $\nu_{127}$) between 1000 and 1100 $cm^{-1}$ and two calculated sets of bands above 1600 $cm^{-1}$ ($\nu_{172}$ and $\nu_{176}$) for both compounds (Table S4, Supporting Information). This qualitative analysis is consistent with the general distribution of modes observed in the spectrum, with dominant intensities arising in the metal−ligand vibrational region (<600 $cm^{-1}$).

A more quantitative approach to assigning the electronic transitions and RR bands was also considered using quantum chemical calculations to estimate the excited-state dimensionless displacement parameters ($\Delta$) for each vibrational mode in each excited state. The expressions for RR intensities as a function of $\Delta$ are well established,[61,62] and the theoretical RR spectra can be predicted using the electronic transition energies obtained from the TD-DFT calculations; theoretical excitation wavelengths used to generate the calculated spectra were adjusted for the applied −2700 $cm^{-1}$ energy shift of the TD-DFT results, as mentioned above. Comparison of the calculated and experimental frequencies of **1** in conjunction with the enhancement patterns facilitates normal mode assignments (Table S4 and Figure S7, Supporting Information). Access to RR spectra obtained at multiple excitation wavelengths further improves this approach; here, we present results based on two experimental excitation wavelengths (488 and 514.5 nm, Figure S1, Supporting Information). In the case of **1**, contributions from three overlapping electronic transitions (States 4, 5, and 6) are observed in the RR spectra. Semiquantitative agreement between theoretical and experimental RR spectra can be obtained for **1** using a linear combination of the predicted RR spectra for all three excited states (Figure 5, bottom, and Figure S8, Supporting Information).

This is a rather simplified approach for predicting an RR spectrum that is obtained in resonance with several states. However, a complete fit to resolve individual contributions to the RR spectrum from different electronic states would suffer from significant ambiguity in the fitted values of electronic transition moments and transition energies due to the significant overlap of electronic bands and limited accuracy of the calculated $\Delta$s. In this approach, we assume that the contribution from the lower energy state is larger in the spectra obtained with the lower energy excitation wavelength, as expected. This method also neglects possible interference effects between the states, though the good correspondence between experiment and theory suggests these effects will not significantly perturb the analysis. It should also be noted that because RR spectral intensities approximately scale as $\Delta^2\nu^2$, predicted relative intensities of low-frequency modes with large deltas are more reliable than predicted intensities of high-frequency modes. In the latter case, the intensities of modes with $|\Delta| \approx 0.1$, which is on the order of the accuracy limit of the theoretical method,[28] can be significantly over- or underestimated in the calculations due to the large frequency prefactor.[61] To account for this, an alternative means for comparison of experiment and theory involves scaling the resonance Raman intensities by the Raman shift $\nu^{-1}$. In this approach, the scaled relative RR intensities are proportional to $\Delta^2\nu$, which is a direct measure of the relative energetic relaxation along the corresponding normal coordinate on the excited state potential energy surface within the IMDHO model. This approach is illustrated in the Supporting Information (Figures S8 and S9), and it is readily apparent that the low-frequency modes dominate the spectra. Overall, despite the approximations made in this analysis, the theoretical results generally support the experimental spectra.

*Theoretical Prediction of Absorption and Resonance Raman Spectra of 2.* The TD-DFT calculations of the absorption spectrum of **2** do not reproduce the experimental spectrum as well as for **1** (Figure 6, top, and Figure S10, Supporting Information). The decomposed experimental bands are broad, which likely reflects contributions from both isomers, for the calculated transition energies are distinct for both conformations. TD-DFT calculations performed for **2** at the geometries obtained from X-ray diffraction results as well as the BP86-optimized geometry indicated changes in the predicted transition energies (Table S5, Supporting Information) with respect to those calculated for the B3LYP-optimized geometry, thus implying that these transition energies are sensitive to small geometric perturbations. However, the changes in geometry otherwise did not significantly affect the character of the transitions (Table S5, Supporting Information). A rough assignment of the decomposed experimental bands to the calculated transitions can be made (Table S6, Supporting Information). The primary visible transition is assigned to State 2/2′, which dominantly reflects nickel charge transfer to the sulfur atoms on the $pdt^{2-}$ ligand and the phosphorus atoms on the dppe ligand (Figure S11, Supporting Information); this electronic transition of **2** resembles State 4 in **1**. From this transition difference density, similar modes are expected to be enhanced in **1** and **2**, including metal−ligand-dominated modes, which is consistent with the similarities in the experimental RR spectra. Additionally, because the electron density on nickel changes significantly, the electron density for the nickel−hydride bond will likely change and modes involving hydride displacement should be enhanced, as observed experimentally. The hydride-to-nickel charge transfer band is predicted to occur at low energies, 15 500 $cm^{-1}$, with very small oscillator strength ($f$ = 0.00035); lack of observed absorption features for **2** at wavelengths greater than 550 nm preclude observation of Raman bands in resonance with that transition.


dx.doi.org/10.1021/ic3017276 | *Inorg. Chem.* 2012, 51, 11787−11797

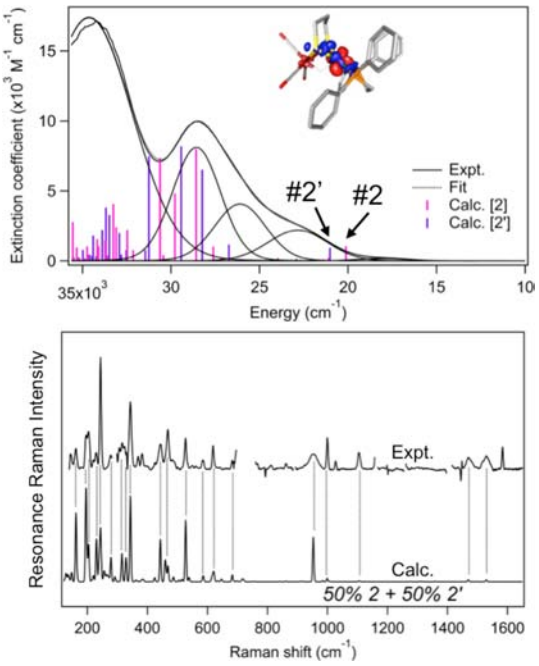


**Figure 6.** (Top) Decomposed absorption spectrum of **2** and calculated TD-DFT transition energies for **2** (pink) and **2′** (purple). Positions of State 2 for each isomer indicated on the graph; difference density contour plot for State 2 shown. Negative electron density in electronic transition is represented by red lobes; positive electron density is represented by blue lobes. (Bottom) Experimental (488 nm ex.) and calculated RR spectrum of **2**; calculated spectrum represents a superposition of **2** and **2′** in equal ratios.

Detailed analysis of the RR spectra of **2** was carried out using predicted intensities obtained for excitation into State 2. The enhancement patterns for **2** and **2′** are very similar, and mode assignments for bands not sensitive to isotopic exchange were assigned by comparing experimental and predicted intensities as described above for the analysis of **1**, with a one-to-one contribution from each isomer used to create the simulated RR spectrum (Figure 6; Table S7 and Figures S12 and S13, Supporting Information). The most significant deviation between experiment and theory occurs in the underestimated intensities of the high-frequency $\nu_{182}$ and $\nu_{CO}$ modes. The corresponding Δs for these modes are 0.1 and 0.05, respectively, and the deviation between the calculated and the experimental intensities corresponds to an underestimation of Δ by 0.1−0.2, which is close to the error of the theoretical method. This error can be related to an underestimation of the excited state delocalization on the Fe−H and CO entities. Likewise, the delocalization of the excited state onto the phenyl substituents of the dppe ligand appears underestimated, which results in lower predicted intensities for the phenyl modes than observed experimentally. Despite these differences in the high-frequency region of the spectra, there is good agreement between the low-frequency calculated and the observed mode frequencies and intensities, which, as shown in the scaled $\nu^{-1}$ representation (Figure S14, Supporting Information), demonstrates that this approach is valid to understand the nature of the excited states of **2**.

*Anharmonic Corrections to the Metal−Hydride Potential Energy Surfaces and Stretching Frequencies.* As noted above, the difference between the calculated and the experimentally observed Ni−H bond length is greater than generally anticipated for metal−ligand bonds.[58] Furthermore, the Fe−H bond stretching frequency is overestimated by more than the usual B3LYP error of ∼4%.[51,52] Discrepancies of this size have previously been observed in calculations on metal−hydride and metal−hydrogen compounds and are generally attributed to the anharmonicity of the potential energy surface (PES) along the metal−hydride or metal−hydrogen bond.[63] In the case of a very anharmonic potential, the calculated geometry, which reflects the minimum along the PES, may not coincide with the expectation value of the nuclear wave function, which is the experimentally observed parameter. To assess the anharmonicity of the metal−hydride vibrational modes, ground state potential energy scan calculations were carried out along the ground state potential energy surfaces for $\nu_{111}$ and $\nu_{182}$, the Ni−H and Fe−H stretching modes (Figures S15 and S16, Supporting Information). It is found that the Ni−H stretching mode exhibits a very soft potential well that deviates significantly from the calculated harmonic potential. In related metal−dihydrogen complexes, exceptionally anharmonic potential energy surfaces have been observed which cause significant variations in calculated H−H distance (up to 0.6 Å).[64] These large anharmonic effects seem to be an intrinsic feature of metal−hydride systems due to the interplay of a relatively small metal−hydride force constant and significant vibrational amplitude in the ground vibrational state. Transforming this dimensionless amplitude into Cartesian coordinates reflects the reduced mass of the mode;[28] thus, the amplitude of a CO stretching mode ($\nu_{183}$) in the ground vibrational state is 0.04 Å, while the amplitude of the Ni−H vibration ($\nu_{111}$) is 4-fold larger (0.17 Å) due to the much smaller reduced mass. A higher vibrational amplitude brings the bond closer to the dissociation limit, and therefore, contributions from anharmonic effects are more significant. The Fe−H stretching mode ($\nu_{182}$) also exhibits significant anharmonicity (Figure S16, Supporting Information), though the geometric coordinate is more rigid. Similarly, the corresponding Cartesian mode amplitude is also large (0.14 Å).

The anharmonic force constants were obtained from a fit of the calculated potential energy surface as described in the Supporting Information. The anharmonic correction to the Ni−H frequency is calculated to be negligible, consistent with the general agreement between the calculated and the observed frequencies (Table 1). Calculations of the Fe−H stretching mode, however, predict a large anharmonic correction factor of around −100 cm$^{-1}$. Therefore, the substantial deviation between the calculated harmonic and the experimental frequencies (approximately −140 cm$^{-1}$) can be accounted for by considering the significant anharmonic correction term to the fundamental frequency. This analysis indicates that in cases where the nuclear displacement along a given vibrational mode is large, as can be expected for metal−hydride stretching vibrations, anharmonicity of the potential energy surface should not be neglected.

Analysis of the anharmonicity of the potential energy surface can also provide the expectation value of the metal−hydride distances. It was found that while the potential energy surfaces for $\nu_{111}$ and $\nu_{182}$ are shallow, the expectation values for both the Ni−H and the Fe−H distance coordinates do not deviate significantly (0.02 Å, Table S8, Supporting Information) from the geometry-optimized parameters. However, it is noted that the cumulative impact of including anharmonic mode couplings for all soft coordinates, including those with significant Ni−Fe


dx.doi.org/10.1021/ic3017276 | *Inorg. Chem.* 2012, 51, 11787−11797

displacement, may lead to noticeable differences between the expectation and the equilibrium geometries.

## DISCUSSION

**Asymmetric Metal−Hydride Bonding.** To the best of our knowledge, this study represents the first detailed analysis of the vibrational modes of a hydride that bridges two different metals. Identification of unambiguous, isotope-dependent bands that can be assigned to local $\nu_{Fe-H}$ and $\nu_{Ni-H}$ stretching vibrations reflects the asymmetry of the bridging hydride within the metal core. This asymmetry decouples the metal−hydride vibrations, which results in two well-separated metal−hydride stretching vibrations rather than coupled symmetric and antisymmetric stretching vibrations. As both the crystal structure and the DFT-optimized geometry indicate distinct metal−hydride bond distances (Table S1, Supporting Information), the observed difference in frequency between the iron−hydride and the nickel−hydride stretching vibrations indicates that this asymmetry is neither a crystallographic nor a computational artifact, and the hydride electron density is unequally distributed between the two metals. Here, we observe that these slight differences in bond length (~0.2 Å) give rise to a large experimental metal−hydride stretching frequency difference of over 500 $cm^{-1}$. In comparison, only a difference of 200 $cm^{-1}$ is predicted for the asymmetric/symmetric Fe−H−Fe stretching vibrations of a [FeFe] hydrogenase model compound.[26] Considering the anharmonicity of the metal−hydride potential energy surface, both the vibrational frequencies and the geometry of **2** can be predicted relatively accurately. Therefore, it may be possible to establish a straightforward correlation between the metal−hydride stretching frequencies and the geometry or symmetry of a molecule containing a bridging hydride.

While Badger's rule,[65] which provides an empirical correlation between force constant/vibrational frequency and bond length, has been successfully applied to determine the geometries of simple inorganic molecules[66] and even iron−oxygen geometries in bioinorganic systems,[67] attempts to characterize metal−hydride bond lengths have not been met with much success.[68] For **2**, Badger's rule predicts iron−hydride bond lengths of 1.76 Å and nickel−hydride bond lengths of 2.17 Å, both of which are significantly greater estimates than those observed in the crystal structure or DFT results. This suggests that metal−hydride bonds may either require different parametrization constants or even fall outside of these standard relationships, though much more data is required to determine this. Toward this end, spectroscopic characterization of additional hydride-bridged bimetallic compounds is underway.

**Vibrational Line Width of Metal−Hydride Bands.** The vibrational bands representing the metal−hydride stretching vibrations were analyzed in detail. The frequency decrease upon isotopic substitution for both isomers **2** and **2′** amounts to almost exactly a factor of $\sqrt{2}$, as predicted by Hooke's law for a diatomic harmonic oscillator. This corroborates the calculated displacements, which indicate that the mode can be accurately described as a localized stretch rather than a delocalized molecular normal mode. Additionally, it is observed that both the iron−hydride and the nickel−hydride stretching vibrations are significantly broadened as compared to the metal−ligand and ligand-centered bands; the Gaussian widths of $\nu_{182}$ and $\nu_{182'}$ are found to be 24 and 22 $cm^{-1}$, respectively (Table S2, Supporting Information). This line width likely results from ensemble effects on the force constant, as shown in eq 1

$$(\nu + \delta\nu) = \sqrt{\frac{(k + \delta k)}{\mu}} \quad (1)$$

where $\delta k$ is the variation of the force constant for a given molecule within the ensemble and $\delta\nu$ is the corresponding variation in vibrational frequency. This equation can be expanded in a Taylor series to show that for a given $\delta k$, $\delta\nu$ will be inversely proportional to the square root of the reduced mass, $\mu$

$$\delta\nu = \frac{1}{2}\frac{\delta k}{\sqrt{\mu k}} \quad (2)$$

It is apparent that the same relationship holds between the statistical standard deviations $\sigma_k$ and $\sigma_\nu$, corresponding to parameters $k$ and $\nu$, respectively. The standard deviation $\sigma_\nu$ determines the amount of inhomogeneous broadening in the vibrational line shape.

Because the reduced masses of the metal−hydride stretching vibrations are near unity due to the localized vibration and low mass of the hydride, this broadening is particularly pronounced. In contrast, for normal modes which represent coupled displacements of several nuclei, $\mu$ is typically much larger and therefore the observed $\sigma\nu$ is necessarily lower, even for equivalent $\sigma k$ values. Accordingly, the $\nu$(Fe−D) bands should be narrowed due to a near 2-fold increase in $\mu$. Assuming equivalent force constants as well as equal variability in the force constant, the line width should decrease by a factor of $\sqrt{2}$. For the primary $\nu$(Fe−D) band $\nu_{182}$, the observed line width decrease from 24 to 18 $cm^{-1}$ is consistent with this analysis. The second $\nu$(Fe−D) band $\nu_{182}'$ also exhibits a smaller line width; the factor by which it narrows is larger than $\sqrt{2}$, but due to the weaker band intensity this value is less well defined. The Ni−H vibration $\nu_{111}$ at 953 $cm^{-1}$ can be decomposed into a single Gaussian peak with a line width of 31 $cm^{-1}$ or two peaks at 945 and 961 $cm^{-1}$ with linewidths of 25 and 22 $cm^{-1}$, respectively, which are very similar to the fwhm values of the $\nu$(Fe−H) bands in the corresponding isomers. Since two $\nu$(Fe−H) bands are observed, decomposition of the broad 953 $cm^{-1}$ band into two overlapping $\nu$(Ni−H) stretching vibrations is consistent with other conclusions.

The observation of broad metal−hydride vibrational bands is not unexpected. Metal clusters containing hydride bridges have historically been known to exhibit weak, broad $\nu$(M−H) modes in both Raman and IR spectroscopies that are often obscured at room temperature.[69,70] These bands have been noted to narrow upon isotopic substitution,[71] and the broad character of the band has even been used to identify the metal−hydride modes.[69] The molecules for which these bridging hydride stretching vibrations have been systematically characterized consist of large, polynuclear clusters with many bridging hydrides and carbonyl ligands, which complicates spectroscopic analysis because normal modes containing metal−hydride displacements overlap and may mix with carbonyl stretching modes. Thus, this broadening was not addressed in a quantitative fashion before. From the simple analysis presented above, we can conclude that metal−hydride bands should be inherently broad, which is a characteristic that should be considered in the analysis of vibrational spectra of related catalytic intermediates or hydrides occurring in biological systems.

**Relevance toward the Study of NiFe Hydrogenase Protein Active Sites.** This study provides a foundation for


dx.doi.org/10.1021/ic3017276 | Inorg. Chem. 2012, 51, 11787−11797

future studies of the protein active site within the [NiFe] hydrogenases. A correlation between metal−hydride frequency and bond distance would have direct relevance for the study of the reduced states, which are proposed to have a bridging hydride ligand with varying amounts of asymmetry.[5,8,72] In the Ni−C state of the standard hydrogenases, the iron−hydride and nickel−hydride bond lengths are 1.7 and 1.6 Å, respectively, as determined by EPR and DFT studies, though this asymmetry is proposed to be increased in the oxygen-tolerant hydrogenases.[5,72] The exact structure of the Ni−R state is still unknown.[6] Observation of the iron−hydride and nickel−hydride stretching frequencies in each state may enable development of a model for the structure of Ni-R using the Ni−C frequencies for validation. This finding would facilitate understanding of the structural and functional differences between these two critical catalytic intermediates.

RR studies of **1** and **2** reveal additional implications for the study of metal−hydride intermediates in hydrogenases. The electronic transitions of **1** that are responsible for the visible absorption bands include charge transfer states onto the bridging sulfur ligands and the terminal carbonyl ligands on Fe, which may be analogous to possible transitions in the protein; therefore, similar transition energies may be anticipated. However, the RR spectra also contain sharp bands from the phenyl substituents on the phosphine ligand. Analogous absorption or vibrational bands will be absent in studies of the protein, and high-frequency bands may be more challenging to identify. From the TD-DFT calculations, it is apparent that the visible electronic transitions in **2** affect the metal−hydride bond because of decreased electron density on the nickel center, but the dominant transition probed in this experiment is not localized on the hydride directly; the corresponding hydride-to-metal charge transfer band occurs with very low intensity. It is therefore possible that an analogous situation is present within the protein: The lower lying electronic transitions in the Ni−R state may not impact bonding in the hydride bridge; in this case, the isotope-sensitive bands would not be resonantly enhanced. This would impede observation of these bands using RR spectroscopy. Additionally, this work reveals that one anticipated characteristic of metal−hydride vibrational bands is an inherently large inhomogeneous line width resulting from the low reduced mass. A broad band with weak intensity will present experimental challenges for detection, which may explain the absence of such studies on protein systems.

TD-DFT calculations coupled with RR intensity predictions can yield insight into relevant electronic excited states and mode assignments, as demonstrated here. This technique would be particularly advantageous in situations when isotopic substitution, the conventional method for normal mode assignments, would be prohibitively costly, as is often the case in protein expression and extraction. The advanced spectral analysis performed on these models represents one of the first detailed theoretical RR studies on a bimetallic compound lacking major symmetry elements, and the agreement between experiment and theory indicates that this approach could be applied to systems as complex as protein active sites, which possess little or no inherent symmetry. Therefore, with sensitive instrumentation and careful choice of excitation wavelength, RR studies coupled with DFT calculations could provide invaluable information on the electronic properties and structure of reduced hydrogenase states.

## CONCLUSIONS

Resonance Raman spectra of compounds **1** and **2**, which are functional and structural models for the Ni−SI and Ni−R states of [NiFe] hydrogenases, respectively, exhibit a rich manifold of vibrational bands. Isotopic substitution of the bridging hydride facilitates mode assignment, and distinct localized metal−hydride stretching vibrations of **2** and its pdt-inverted isomer **2′** are identified at 945 and 960 $cm^{-1}$ and 1528 and 1470 $cm^{-1}$ for the $\nu$(Ni−H) and $\nu$(Fe−H) modes of **2** and **2′**, respectively. DFT and TD-DFT calculations have enabled identification of the dominant electronic excited states probed in these experiments. Furthermore, normal mode gradient calculations predict RR enhancement patterns that are in reasonable agreement with the experimental spectra for both **1** and **2**, demonstrating the applicability of the method for the study of large molecules lacking elements of high symmetry. Vibrational line shape analysis indicates that metal−hydride bands will be inherently broadened, particularly for asymmetric metal−hydride bridges; in addition, the asymmetry of the metal−hydride−metal core of a bridging hydride is reflected in the significant difference in vibrational frequencies between the two localized metal−hydride stretching vibrations. Overall, this study provides a framework for characterization of metal−hydride vibrational bands within a bimetallic molecule, which will facilitate possible future RR studies on the [NiFe] hydrogenases in well-defined redox states aiming at a better understanding of the catalytic mechanism of hydrogen production.

## ASSOCIATED CONTENT

### Supporting Information

Supplemental discussions and figures on DFT calculations and inverted $pdt^{2-}$ isomers, table of geometric parameters, excitation wavelength dependence of RR spectra, assignments with figures of electronic transitions and RR modes for **1** and **2**, calculated PESs for metal−hydride normal modes, calculated anharmonic corrections to metal−hydride fundamental frequencies. This material is available free of charge via the Internet at http://pubs.acs.org.

## AUTHOR INFORMATION

### Corresponding Author

*E-mail: wolfgang.lubitz@cec.mpg.de.

### Notes

The authors declare no competing financial interest.

## ACKNOWLEDGMENTS

We thank the Max Planck Society for financial support. H.S.S. gratefully acknowledges support from the Alexander von Humboldt Foundation. Ms. Marion Stapper and Mr. Jan Hanis are gratefully acknowledged for expert technical assistance. K.W. acknowledges the Fonds der Chemischen Industrie for the Doctoral Kekulé Fellowship.

## REFERENCES

(1) Lubitz, W.; Reijerse, E. J.; Messinger, J. *Energy Environ. Sci.* **2008**, *1*, 15.
(2) Kim, D.-H.; Kim, M.-S. *Bioresour. Technol.* **2011**, *102*, 8423.
(3) Lubitz, W.; Reijerse, E.; van Gastel, M. *Chem. Rev.* **2007**, *107*, 4331.
(4) Stein, M.; Lubitz, W. *J. Inorg. Biochem.* **2004**, *98*, 862.
(5) Brecht, M.; van Gastel, M.; Buhrke, T.; Friedrich, B.; Lubitz, W. *J. Am. Chem. Soc.* **2003**, *125*, 13075.

(6) Ogata, H.; Lubitz, W.; Higuchi, Y. *Dalton Trans.* **2009**, 7577.
(7) Foerster, S.; Stein, M.; Brecht, M.; Ogata, H.; Higuchi, Y.; Lubitz, W. *J. Am. Chem. Soc.* **2003**, *125*, 83.
(8) Foerster, S.; Gastel, M. v.; Brecht, M.; Lubitz, W. *J. Biol. Inorg. Chem.* **2005**, *10*, 51.
(9) Fontecilla-Camps, J. C.; Volbeda, A.; Cavazza, C.; Nicolet, Y. *Chem. Rev.* **2007**, *107*, 4273.
(10) De Gioia, L.; Fantucci, P.; Guigliarelli, B.; Bertrand, P. *Int. J. Quantum Chem.* **1999**, *73*, 187.
(11) Tard, C.; Pickett, C. J. *Chem. Rev.* **2009**, *109*, 2245.
(12) Ohki, Y.; Tatsumi, K. *Eur. J. Inorg. Chem.* **2011**, 973.
(13) Barton, B. E.; Rauchfuss, T. B. *J. Am. Chem. Soc.* **2010**, *132*, 14877.
(14) Lai, C.-H.; Reibenspies, J. H.; Darensbourg, M. Y. *Angew. Chem., Int. Ed.* **1996**, *35*, 2390.
(15) Canaguier, S.; Field, M.; Oudart, Y.; Pecaut, J.; Fontecave, M.; Artero, V. *Chem. Commun.* **2010**, *46*, 5876.
(16) Tanino, S.; Li, Z.; Ohki, Y.; Tatsumi, K. *Inorg. Chem.* **2009**, *48*, 2358.
(17) Perra, A.; Davies, E. S.; Hyde, J. R.; Wang, Q.; McMaster, J.; Schröder, M. *Chem. Commun.* **2006**, 1103.
(18) Sellmann, D.; Lauderbach, F.; Geipel, F.; Heinemann, F. W.; Moll, M. *Angew. Chem., Int. Ed.* **2004**, *43*, 3141.
(19) Dubois, M. R.; Dubois, D. L. *Acc. Chem. Res.* **2009**, *42*, 1974.
(20) Barton, B. E.; Whaley, C. M.; Rauchfuss, T. B.; Gray, D. L. *J. Am. Chem. Soc.* **2009**, *131*, 6942.
(21) Higuchi, Y.; Ogata, H.; Miki, K.; Yasuoka, N.; Yagi, T. *Structure* **1999**, *7*, 549.
(22) Zhu, W. F.; Marr, A. C.; Wang, Q.; Neese, F.; Spencer, D. J. E.; Blake, A. J.; Cooke, P. A.; Wilson, C.; Schroder, M. *Proc. Natl. Acad. Sci.* **2005**, *102*, 18280.
(23) Lindahl, P. A. *J. Inorg. Biochem.* **2012**, *106*, 172.
(24) Johnson, M. K.; Czernuszewicz, R. S.; Spiro, T. G.; Fee, J. A.; Sweeney, W. V. *J. Am. Chem. Soc.* **1983**, *105*, 6671.
(25) Fiedler, A. T.; Brunold, T. C. *Inorg. Chem.* **2005**, *44*, 1794.
(26) Galinato, M. G. I.; Whaley, C. M.; Roberts, D.; Wang, P.; Lehnert, N. *Eur. J. Inorg. Chem.* **2011**, *2011*, 1147.
(27) Stromberg, C. J.; Kohnhorst, C. L.; Van Meter, G. A.; Rakowski, E. A.; Caplins, B. C.; Gutowski, T. A.; Mehalko, J. L.; Heilweil, E. J. *Vibr. Spectrosc.* **2011**, *56*, 219.
(28) Petrenko, T.; Neese, F. *J. Chem. Phys.* **2007**, 127.
(29) Mitsuo, I. *Spectrochim. Acta* **1965**, *21*, 731.
(30) Ferraro, J. R.; Nakamoto, K. *Introductory Raman Spectroscopy*; Academic Press: New York, 1994.
(31) Neese, F. *Wiley Interdiscip. Rev. Comput. Mol. Sci.* **2012**, *2*, 73.
(32) Pantazis, D. A.; Chen, X.-Y.; Landis, C. R.; Neese, F. *J. Chem. Theory Comput.* **2008**, *4*, 908.
(33) Pantazis, D. A.; Neese, F. *J. Chem. Theory Comput.* **2009**, *5*, 2229.
(34) Becke, A. D. *Phys. Rev. A* **1988**, *38*, 3098.
(35) Perdew, J. P. *Phys. Rev. B* **1986**, *33*, 8822.
(36) Becke, A. D. *J. Chem. Phys.* **1993**, *98*, 5648.
(37) Lee, C. T.; Yang, W. T.; Parr, R. G. *Phys. Rev. B* **1988**, *37*, 785.
(38) Weigend, F.; Ahlrichs, R. *Phys. Chem. Chem. Phys.* **2005**, *7*, 3297.
(39) Kendall, R. A.; Dunning, T. H.; Harrison, R. J. *J. Chem. Phys.* **1992**, *96*, 6796.
(40) van Lenthe, E.; Baerends, E. J.; Snijders, J. G. *J. Chem. Phys.* **1993**, *99*, 4597.
(41) van Lenthe, E.; Baerends, E. J.; Snijders, J. G. *J. Chem. Phys.* **1994**, *101*, 9783.
(42) van Lenthe, E.; vanLeeuwen, R.; Baerends, E. J.; Snijders, J. G. *Int. J. Quantum Chem.* **1996**, *57*, 281.
(43) Grimme, S.; Antony, J.; Ehrlich, S.; Krieg, H. *J. Chem. Phys.* **2010**, 132.
(44) Grimme, S.; Ehrlich, S.; Goerigk, L. *J. Comput. Chem.* **2011**, *32*, 1456.
(45) Klamt, A.; Schuurmann, G. *J. Chem. Soc., Perkin Trans. 2* **1993**, 799.
(46) Petrenko, T.; Kossmann, S.; Neese, F. *J. Chem. Phys.* **2011**, 134.
(47) Furche, F. *J. Chem. Phys.* **2001**, *114*, 5982.
(48) Neese, F.; Olbrich, G. *Chem. Phys. Lett.* **2002**, *362*, 170.
(49) Petrenko, T.; Ray, K.; Wieghardt, K. E.; Neese, F. *J. Am. Chem. Soc.* **2006**, *128*, 4422.
(50) Ray, K.; Petrenko, T.; Wieghardt, K.; Neese, F. *Dalton Trans.* **2007**, 1552.
(51) Merrick, J. P.; Moran, D.; Radom, L. *J. Phys. Chem. A* **2007**, *111*, 11683.
(52) Wong, M. W. *Chem. Phys. Lett.* **1996**, *256*, 391.
(53) Bertini, L.; Greco, C.; Bruschi, M.; Fantucci, P.; De Gioia, L. *Organometallics* **2010**, *29*, 2013.
(54) Liu, T.; Li, B.; Singleton, M. L.; Hall, M. B.; Darensbourg, M. Y. *J. Am. Chem. Soc.* **2009**, *131*, 8296.
(55) Schilter, D.; Nilges, M. J.; Chakrabarti, M.; Lindahl, P. A.; Rauchfuss, T. B.; Stein, M. *Inorg. Chem.* **2012**, *51*, 2338.
(56) Justice, A. K.; De Gioia, L.; Nilges, M. J.; Rauchfuss, T. B.; Wilson, S. R.; Zampella, G. *Inorg. Chem.* **2008**, *47*, 7405.
(57) Neese, F. *Coord. Chem. Rev.* **2009**, *253*, 526.
(58) Orio, M.; Pantazis, D. A.; Neese, F. *Photosynth. Res.* **2009**, *102*, 443.
(59) Buehl, M.; Reimann, C.; Pantazis, D. A.; Bredow, T.; Neese, F. *J. Chem. Theory Comput.* **2008**, *4*, 1449.
(60) Neese, F. *J. Biol. Inorg. Chem.* **2006**, *11*, 702.
(61) Lee, S. Y.; Heller, E. J. *J. Chem. Phys.* **1979**, *71*, 4777.
(62) Myers, A. B.; Mathies, R. A. In *Biological Applications of Raman Spectroscopy*; Spiro, T. G., Ed.; John Wiley and Sons: New York, 1987; Vol. *2*.
(63) Heinekey, D. M.; Lledos, A.; Lluch, J. M. *Chem. Soc. Rev.* **2004**, *33*, 175.
(64) Maseras, F.; Lledas, A.; Clot, E.; Eisenstein, O. *Chem. Rev.* **2000**, *100*, 601.
(65) Badger, R. M. *J. Chem. Phys.* **1934**, 2128.
(66) Weisshaar, J. C. *J. Chem. Phys.* **1989**, *90*, 1429.
(67) Green, M. T. *J. Am. Chem. Soc.* **2006**, *128*, 1902.
(68) Hagemann, H.; Moyer, R. O. *J. Alloys Compd.* **2002**, *330*, 296.
(69) Kaesz, H. D.; Saillant, R. B. *Chem. Rev.* **1972**, *72*, 231.
(70) Cooper, C, B.; Shriver, D, F.; Onaka, S. In *Transition Metal Hydrides*; American Chemical Society: Washington DC, 1978; Vol. *167*, p 232.
(71) Shapley, J. R.; Keister, J. B.; Churchill, M. R.; DeBoer, B. G. *J. Am. Chem. Soc.* **1975**, *97*, 4145.
(72) Pandelia, M.-E.; Infossi, P.; Stein, M.; Giudici-Orticoni, M.-T.; Lubitz, W. *Chem. Commun.* **2012**, *48*, 823.